JIHE ZHAO [1], JIAXU JIN [1,3*], YANFENG LI [2,4], PENGFEI WU [1], HAIBO WANG [5*], YINGSHUANG SHI [6]

CONSIDERING THE EFFECTS OF LOCAL IMPACT DISTURBANCE ON DEEP SANDSTONE: EXPLORING STRENGTH WEAKENING MECHANISM

The stability of rock mass is an important safety issue in the process of deep mining, and the dynamic disturbance caused by excavation and blasting is an important factor affecting the stability of rock mass. To deeply understand the mechanical characteristics and damage mechanisms of deep sandstone after local impact disturbance by high prestresses, a self-developed rock disturbance system was used to carry out disturbance followed by a uniaxial compression test (UCT) on the rock samples. The whole process of UCT was monitored utilising acoustic emission (AE) technology, and the particle size and fractal dimension of debris after sandstone failure were analysed to explore its strength-weakening mechanism. The experimental study elucidated the influence mechanism of the coupled action of disturbance frequency f and impact area s on the strength weakening effect of sandstone, i.e., high prestressing force is the prerequisite and dominant factor of rock strength weakening, while the perturbation f and the s accelerate the induced rock damage. The fractal dimension D can be used to quantitatively evaluate the fragmentation characteristics of sandstone disturbed by local impact (between 1.68 and 2.14), and it shows a good linear increasing trend with the increase of local impact disturbance.

Keywords: Deep sandstone; local impact disturbance; uniaxial compression; acoustic emission; fractal dimension

[1] LIAONING TECHNICAL UNIVERSITY, COLLEGE OF CIVIL ENGINEERING, FUXIN 123000, CHINA
[2] SHENYANG JIANZHU UNIVERSITY, SCHOOL OF TRANSPORTATION AND GEOMATICS ENGINEERING, SHENYANG 110168, CHINA
[3] LIAONING KEY LABORATORY OF MINE SUBSIDENCE DISASTER PREVENTION AND CONTROL, FUXIN 123000, CHINA
[4] NORTHEASTERN UNIVERSITY, KEY LABORATORY OF THE MINISTRY OF EDUCATION ON SAFE MINING OF DEEP METAL MINES, SHENYANG 110819, CHINA
[5] ANHUI UNIVERSITY OF SCIENCE AND TECHNOLOGY, ANHUI KEY LABORATORY OF MINING CONSTRUCTION ENGINEERING, HUAINAN, ANHUI, 232001, CHINA
[6] COLLEGE OF SCIENCE, NORTH CHINA INSTITUTE OF SCIENCE & TECHNOLOGY, YANJIAO, 065201, CHINA

* Corresponding author: jjx_605@163.com

1. Introduction

As shallow mineral resources are depleted in various countries, mining is gradually extending into deeper underground spaces. Compared with shallow rock, deep rock is confined to a specific high-stress environment and runs through the whole excavation process [1,2]. However, in the process of deep excavation, the rock is inevitably subject to dynamic disturbances such as mechanical vibration, blasting operations, and seismic shocks [3-6]. Dynamic load has both positive and negative effects: on the one hand, it is used to transform reservoir permeability, and efficient rock breaking to improve mining efficiency; on the other hand, they are prevented from damaging the rock structure due to dynamic loads, and the collapse and other disasters in a certain range caused by deep mine operation occur frequently [7-10]. Therefore, it is of great significance for the design and safe construction of deep rock engineering to understand the failure characteristics and mechanisms of deep rock structures after experiencing dynamic disturbance.

In recent years, many scholars have studied the mechanical properties of different types of rocks under disturbance, which greatly promoted the development of rock mechanics theory. Li et al. [11] showed that when the axial preloading stress exceeds 70% of the uniaxial compressive strength (UCS), the strength of the siltstone specimen under impact load will decrease rapidly. Gong et al. [12] studied the mechanical properties of red sandstone under impact disturbance when the prestress is 52%, 70% and 78% UCS, and found that with the increase of axial compression ratio, the strength will increase first and then decrease, which confirmed the rockburst phenomenon of prestressed red sandstone under impact disturbance. Luo et al. [13] considered the mechanical behaviour and acoustic emission (AE) characteristics of rock failure induced by light, medium and weak dynamic disturbances, and established a new elastoplastic damage constitutive model. Zhou et al. [14] used a customised SHPB device to carry out impact tests on the rock under different dynamic-static load coupling and studied the dynamic compression and tension behaviour of sandstone. Li et al. [15] performed uniaxial compression tests using a split Hopkinson pressure bar device driven by a pendulum to examine the degradation process of green sandstone under repetitive impact loading. The above studies mainly focus on the deformation characteristics and mechanical properties of rock under impact and cyclic loading. However, in actual deep mining, due to the influence of geological structure, artificial excavation, hydraulic fracturing, etc. [16], or the roof fracture and local vibration blasting during mining, the roadway and chamber in the rock mass are often frequently disturbed by local impact loading [17]. Therefore, it is impossible to solve the problem of damage and failure of rock mass under high prestress and local dynamic impact in practical engineering according to the conventional full-contact impact test model (the action area of dynamic impact coincides with the end face of the specimen). Up to now, there are few experimental studies on deep rock considering the influence of disturbance frequency f and impact area s, i.e., under the condition of high prestress, rock is accompanied by local impact disturbance, and the law of strength weakening and damage failure is explored.

Scholars have found that the macroscopic fragmentation of rock is the final result of the continuous initiation, development, expansion, aggregation and coalescence of its internal defects, and the process from meso-damage to macroscopic fragmentation has fractal properties [18-20]. Liu et al. [21] used acoustic emission and CT scanning techniques to analyse the fracture evolution of freeze-thaw granite with natural cracks under uniaxial and multi-stage cyclic loading. Lai et al. [22] carried out uniaxial compression tests on rocks at different loading rates, and compared and analysed the fractal dimension of rock macro-fragmentation and the fractal characteristics of meso-fracture morphology through fractal theory and scanning electron microscope (SEM).

To study the mechanical behaviour of shale under the uniaxial compression test, Wang et al. [23] used two fractal dimensions of fragment size distribution *Fs* and surface crack distribution *Fb* to explain the relationship between shale mechanical properties and fractal dimension. Through experimental verification, it is found that the fragmentation process has self-similarity with the shape of rock blocks, and the size distribution of fragments shows power-law characteristics, which is called fractal in statistics. At the same time, the analysis of rock microstructure shows that the pores and fissures of the rock are fractal distribution, and the fragments are the direct result of the expansion of the fissures. Therefore, to reveal the failure law of deep rock, this study is of great engineering guiding value.

To sum up, to clarify the influence of local impact disturbance on deep sandstone, i.e., the mechanical properties and failure characteristics of sandstone under the action of high prestress and coupling, the self-developed rock disturbance system is used to carry out the uniaxial compression test (UCT) on sandstone specimens after disturbance. On this basis, the influence of local impact disturbance on the strength weakening degree, the fractal dimension of fragments and the damage evolution law of deep sandstone are explored, and the research results provide a new way to explore the inherent law between the fractal characteristics of local impact disturbance fragmentation and mechanical properties of deep rock. It has significant theoretical significance and engineering guiding value for the identification and control of dynamic disasters in deep mines.

2. Testing

2.1. Material preparation and scheme

Deep rock engineering often chooses to construct permanent structures in sandstone strata (TABLE 1). According to the deep rock engineering specimens with sandstone as the main body, red sandstone, green sandstone, and purple sandstone with fine and uniform grains, dense texture, intact structure, and a buried depth of about 800 m are selected. The composition of each sandstone is determined by optical microscopic testing technology.

TABLE 1

Deep rock engineering with sandstone as the main body

Name	Location	Lithology	Year	Compressive strength/MPa	Buried depth/m	Position
Darley Dale	UK	Sandstone	2009	155	850	—
Shuijingtou Coal Mine	HN, CN	Sandstone	2012	45.57	615	Coal mine roadway
Zhujidong Coal Mine	AH, CN	Sandstone	2018	103.15	906	Coal mine roadway
Kunchuan-Tibet Railway	Tibet, CN	Sandstone	2021	40.95	850	—

Red sandstone is mainly composed of quartz, potassium feldspar, illite, calcite and other minerals (Fig. 1(a)); green sandstone is primarily composed of quartz, feldspar and other minerals, and biotite auxiliary minerals (Fig. 1(b)); purple sandstone is mainly composed of hematite, quartz, hydromica and other minerals (Fig. 1(c)). They were processed into $50 \times 50 \times 50$ mm (Fig. 2(a)) specimens according to the ISRM test procedure [24-26]. An electronic weighing scale was used to reduce the error (Fig. 2(b)), a vernier calliper was used to measure the size and flatness

(Fig. 2(c)), and a wave velocity meter was used to measure the wave velocity (Fig. 2(d)). The average UCS of the specimen was determined through multiple UCTs, and the specimens with the same physical and mechanical properties were selected for the test, as shown in TABLE 2. The research results can provide a reference for the subsequent UCT of sandstone disturbed by the local impact of high prestress. To minimise the impact of temperature fluctuations on the test, it is conducted in a room with a constant temperature of 23±2°C.
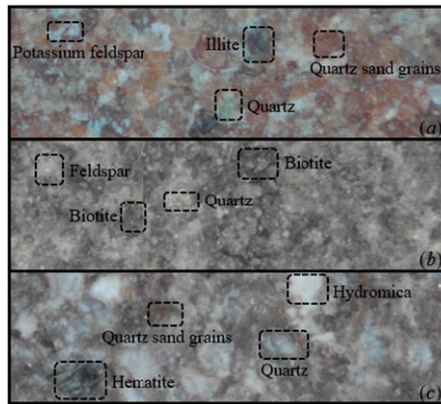

Fig. 1. Mineral composition: red sandstone (a), green sandstone (b), purple sandstone (c)

TABLE 2

Physical and mechanical parameters of specimens

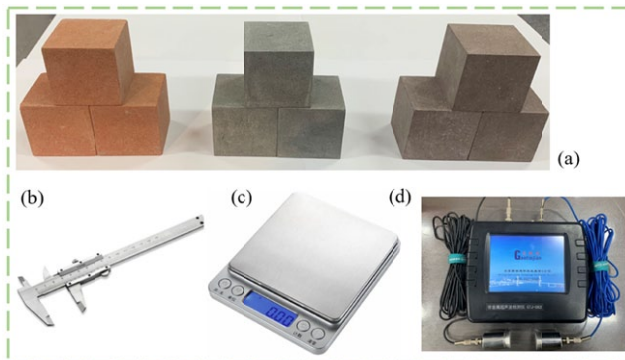| Name	Density /g·cm^{-3}	Compressive strength /Mpa	Tensile strength /Mpa	Cohesion /Mpa	Internal friction angle/°	Elastic modulus /Gpa	Poisson ratio
Red sandstone	2.36	45	6	20.5	24.4	30.6	0.26
Green sandstone	2.65	100	9	63.3	31.8	32.8	0.28
Purple sandstone	2.82	150	12	108.9	36.0	34.7	0.29

Fig. 2. Sandstone specimen (a), electronic scale (b), vernier caliper (c), wave velocity meter (d)

The dynamic disturbance of high-prestressed sandstone is divided into the static loading and the local impact disturbance stages. When the principal compressive stress reaches a predetermined value, the lateral compressive stress is subjected to cyclic dynamic loading. To simulate the elastic wave in the process of vibration propagation, the cyclic disturbance waveform is presented in the form of a sine wave and the loading process and characteristics are shown in Fig. 3 σ_{3max} and σ_{3min} are the upper and lower limit stresses of the cyclic load, respectively, $\Delta\sigma = \sigma_{3max} - \sigma_{3min}$ is the disturbance amplitude, and T is the loading period. In addition, σ_1 was set to 16 MPa due to the deep location of the rock, three different disturbance frequencies f of 3, 5, and 7 Hz were used, and the impact area s was set by impacting the sandstone surface with three different sizes of impact heads, 0.12 s, 0.07 s, and 0.03 s, respectively, for 30 minutes. Test conditions of specimen with code 16R3-7 (i.e., 16 represents the principal stress of 16 MPa, 3 represents the disturbance frequency of 3 Hz, 7 represents the impact area of 0.07 s, R represents the red sandstone, G represents the green sandstone, and P represents the purple sandstone) are listed.

It must be recognized that the local impact disturbance test of high-prestressed rock in this work is not a fatigue test. The influence of high prestress level, disturbance frequency and impact area on the strength of rock is studied, rather than the influence of disturbance on the fatigue life, which is a concern in the fatigue test. It must be reiterated that testing is fundamentally different from fatigue testing, focusing on the changing characteristics of strength rather than fatigue life.
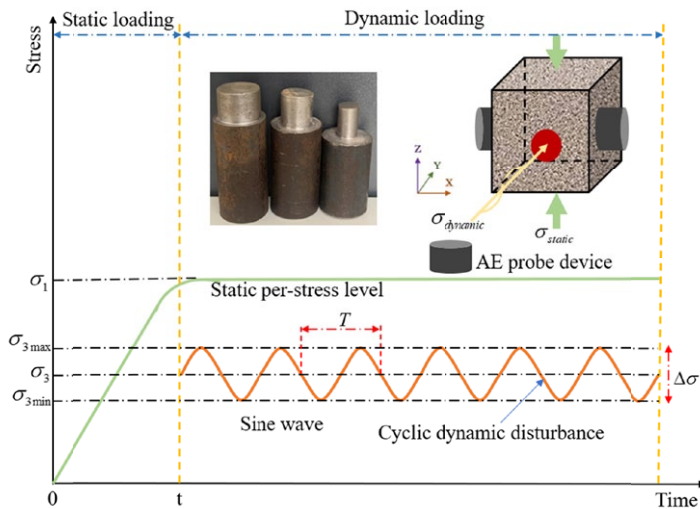

Fig. 3. Test loading process and characteristics

2.2. Testing equipment and procedures

The local impact disturbance test equipment shown in Fig. 4 is mainly composed of a WDW-100E single-axis servo-hydraulic loading system, data monitoring system and self-made disturbance loading system. It is worth noting that the disturbance loading system consists

of two important parts: the SRMCO-VM05 frequency converter is a silent, high-performance, multi-functional universal inverter with a power of 2200 W and a rated voltage of 380 V; The YE3-80M1-2 three-phase asynchronous motor is an additional vibration motor with a power of 750 W, a rated voltage of 380 V and a frequency of 50 Hz. The motor drives the impact connecting rod of the eccentric wheel structure to disturb. The impact head uses spring links to prevent friction between the specimen and the plane. The expansion rivet is used to fix the self-developed disturbance loading device to the ground to ensure the impact load is the same.
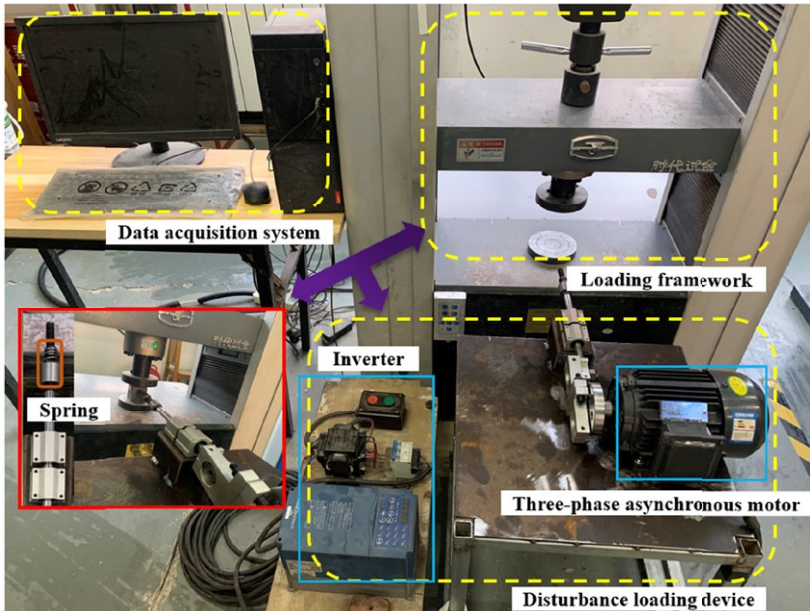

Fig. 4. Self-developed local impact disturbance test equipment

The UCT is carried out on the MTS-2000 uniaxial servo-hydraulic testing machine test system, as shown in Fig. 5. The test system is mainly composed of the software control system and equipment loading hardware system, which constitutes a reliable servo-hydraulic closed-loop control equipment system integrated with data acquisition of axial load, axial deformation, time and so on. UCT was carried out on sandstone specimens after local impact disturbance at a constant loading rate of 0.3 mm/min, and acoustic emission signals were monitored synchronously during the loading process. The DS5 acoustic emission system (Softland Times, China) was used for the acquisition of AE signals, the threshold was set at 40 dB to obtain a high signal-to-noise ratio, the sampling interval was 40 ms, and the sampling frequency was 1000 kHz. The sensor is fixed on the rock surface with adhesive tape, and a layer of Vaseline is applied between the specimen surface and the probe as a coupling agent to ensure good acoustic coupling between the two. The axial compression loading system and the AE monitoring system are synchronously started to monitor and record the AE signals of the whole process from the loading to the destruction of the specimen. It should be noted that all rock samples were subjected to a local impact disturbance process before the test and performed at the same room temperature (23±2°C).
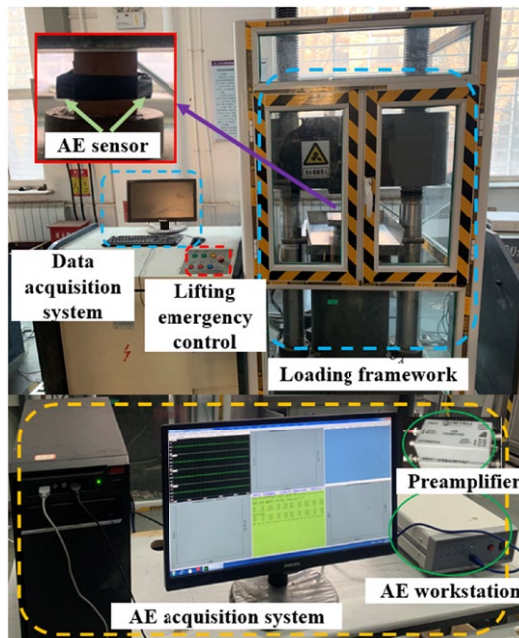
Fig. 5. UCT-AE test equipment

3. UCT Result

Mineral particles and cement in UCT sandstone will break and release energy during loading, resulting in AE signals [27]. At present, it is common to use ringing count and energy to analyze the characteristics of AE time series. Energy reflects the relative energy or intensity of AE events, and the ringing count reflects the intensity and frequency of AE signals [28]. Because the change rule of the energy obtained from the AE test is similar to that of the ringing count, only the AE ringing count is an example to analyse and explain in the study.

3.1. Stress analysis

Figs. 6-8 plots the stress, ringing count, and cumulative ringing count versus time for sandstones of different strengths. The stress thresholds (crack closure stress σ_A, yield stress σ_{cd}, and peak strength σ_p) are identified, and the time-variation of the stresses is divided into four deformation stages, namely, the initial crack compaction stage (I), the elastic deformation stage (II), the unstable crack propagation stage (III), and the failure stage (IV) [29].

Stage I: The axial stress-time curve of the specimen gradually bends toward the stress axis, and some primary pores and cracks close due to the increase of compaction degree. Similarly, crack closure reduces the porosity between mineral particles inside the specimen and enhances the stability of the overall structure of the specimen.

Stage II: When the stress reaches σ_A, the original crack is completely closed. After that, the slope of the stress curve remained basically unchanged, and no failure occurred in the rock.

In this case, if the stress is removed, the specimen can return to its original state, so this stage belongs to the elastic deformation stage.

Stage III: The axial stress has exceeded σ_{cd}, and the slope of the curve increases significantly. Currently, the sandstone specimen shows an expansion effect, resulting in the formation of new cracks inside that develop rapidly. In this static prestress state, the crack density of the specimen sharply increases, leading to a significant deterioration in its mechanical properties.

Stage IV: The axial stress has exceeded σ_p, the sandstone is destroyed due to the formation of transfixion cracks, the bearing capacity decreases rapidly, and the curve shape changes significantly.
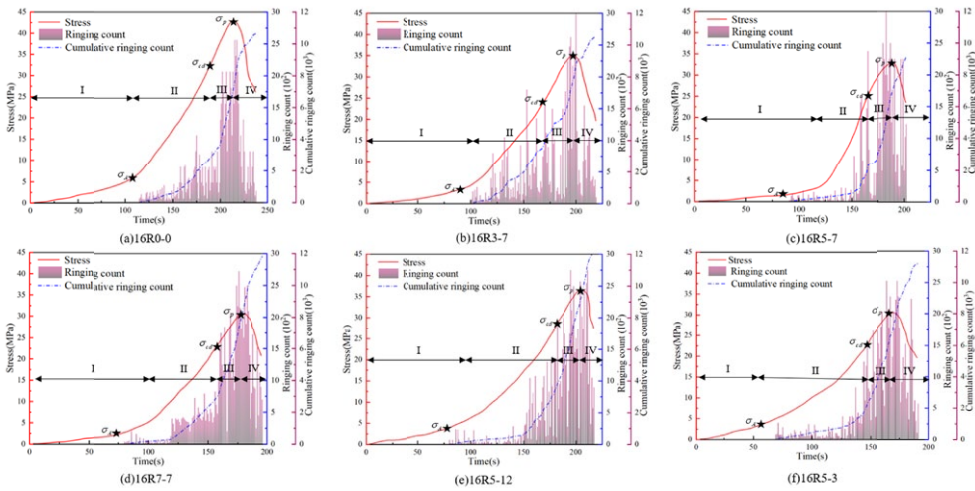

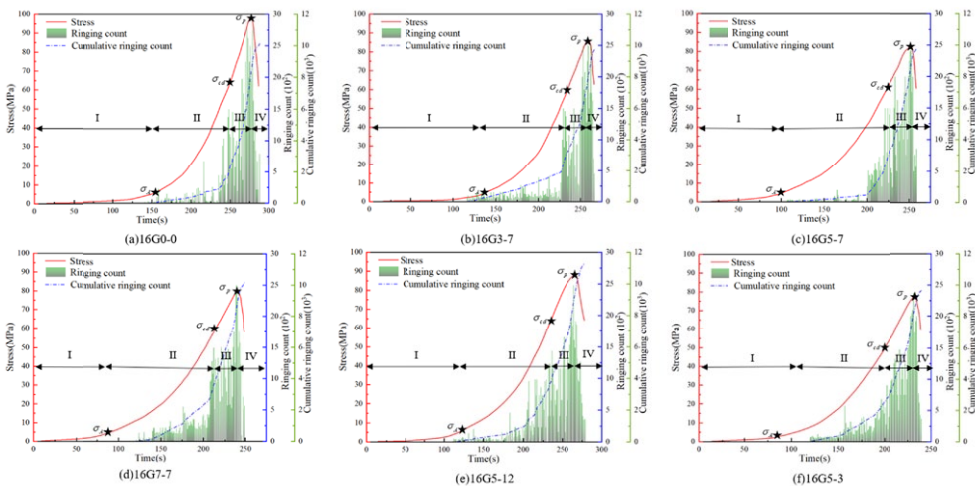Fig. 6. The stress-time-ringing count relationship of red sandstone under different $f - s$

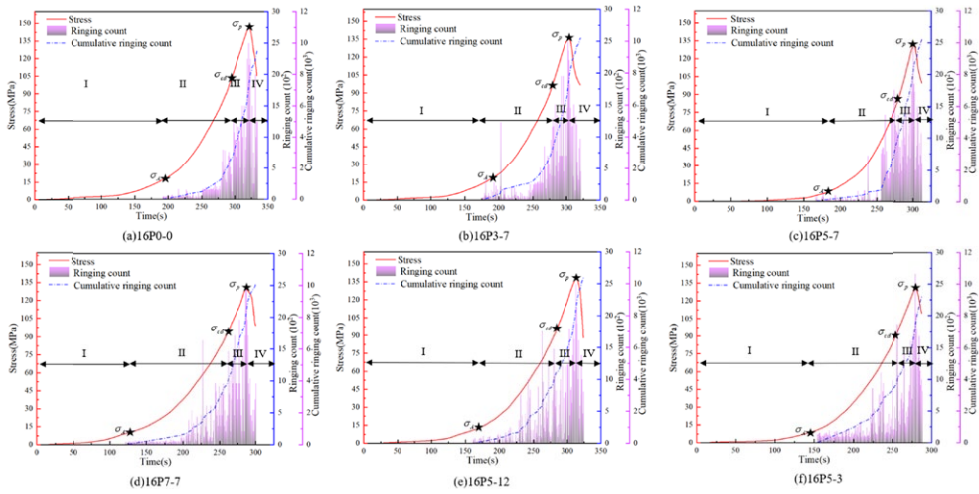Fig. 7. The stress-time-ringing count relationship of green sandstone under different $f - s$

Fig. 8. The stress-time-ringing count relationship of purple sandstone under different $f - s$

When the same σ_1 is applied to the rock sample, sandstone σ_p after local impact disturbance is relatively reduced. When s is the same, σ_p decreases with the increase of f, but when f is the same, the increase of σ_p with s is just the opposite. Under higher prestress, sandstone is more likely to fail along the strike direction after experiencing multiple local impact disturbances. For the disturbed sandstone, the initial micro-defects are compacted first, and the initial crack compaction stage will occur earlier. Due to the decrease of pore space, the mechanical properties of rock are improved. With the increase of stress, these initial micro-defects are completely closed. When the stress exceeds σ_{cd}, the secondary micro-defects undergo the process of crack nucleation, propagation and merger until the rock fails.

3.2. AE Characteristics

During the process of rock failure, parameters such as the acoustic emission (AE) ringing number and energy levels can reflect the degree of failure and the damage evolution process of rock under external loads to a certain extent. AE events can be divided into four stages according to AE ringing count in Figs. 6-8: initial silent period (I), random distribution period (II), aggregated burst period (III) and failure reduction period (IV). AE characteristics of each stage are described as follows:

Stage I: In this stage, there is almost no AE event, the AE ringing count is very small, and the maximum proportion of the cumulative ringing count to the total cumulative ringing count is only 1.53% (16P7-7). Stage I corresponds to the initial crack compaction stage of stress loading, and the stress at the end is σ_A. The observed phenomenon can be attributed to the compact structure of the rock sample, in which the initial micro-cracks have closed. This is indicated by the subtle compaction section in the stress-time curve, which reflects this characteristic. Additionally, the acoustic emission (AE) ringing count shows that the initial crack compaction stage of the specimen occurs earlier after experiencing local impact disturbance. This early compaction stage plays a significant role in the generation of early AE signals [33].

72

Stage II: The early AE events are randomly distributed, and a small number of AE events with small energy are generated. The number of AE rings increases slowly with the increase of stress, and the cumulative number of rings accounts for about 15%-20% of the total cumulative number of rings, which is mainly due to the discreteness of the specimen. Studies have shown that [34] sandstone will produce a small amount of AE signals due to its structural form and intergranular compression deformation, resulting in slow growth of acoustic emission ringing counts and approximately linear growth of cumulative ringing counts. In the later stage, new microcracks have been generated inside the rock sample and damage has gradually appeared, but the energy is still low, and the corresponding stress at the end of stage II is σ_{cd}.

Stage III: When the stress exceeds σ_{cd}, the plastic deformation is accompanied by the unstable propagation of microcracks, the AE ringing count and the cumulative ringing count increase sharply, and the aggregation and explosion phenomenon appears on the time axis. At this stage, the internal cracks of sandstone rapidly form a swelling set, the fracture area forms a damage slip surface, the damage degree is significantly increased, the micro-cracks expand unstably in the rock sample, the main fracture surface is gradually formed, and the bearing capacity is gradually reduced [35]. However, the duration of AE signals of different kinds of sandstones is significantly shortened with the increase of their strength. At the moment when the stress reaches the peak value and drops, the cumulative ringing counts-time curve also rises in a straight line of nearly 90°, and the internal micro-cracks of the rock sample are interconnected to form a macroscopic fracture surface [36].

Stage IV: In the residual stress stage, a large number of micro-cracks are generated in the rock sample, the degree of internal damage is increasing, and instability failure occurs [37]. At the same time, many secondary tensile cracks are produced, and finally, the penetrating macroscopic fracture is formed. The movement of the fracture still produces a large number of AE signals. However, the AE ringing count decreased, and the cumulative ringing count increased significantly.

3.3. Strength weakening effect

TABLE 3 shows the strength of different types of sandstone specimens after local impact disturbance and the difference between UCS and σ_p. Under the condition of $A = 16$ MPa (36% UCS), the red sandstone specimens disturbed by local impact are reduced by 8.52~14.77 MPa compared with monotonic loading (UCS = 45 MPa). Similarly, the strength of green sandstone and purple sandstone is reduced by 11.76~22.98 MPa and 12.78~20.93 MPa, respectively, which fully indicates that the strength of sandstone specimens subjected to high prestress local impact disturbance is weakened, showing an obvious strength weakening effect. To describe this effect quantitatively, the strength-weakening rate (SWR) is proposed. The SWR is defined as follows [38]:

$$SWR = \frac{UCS - \sigma_p}{UCS} \times 100\% \tag{1}$$

Through the analysis of SWR value, it can be seen that when the same σ_1 is applied, the change of the strength of the specimen under different $f - s$ is different. Under the condition of small frequency ($f = 3$ Hz) or large impact area (0.12 s), the strength of the specimen under σ_1 stress level is similar to that of UCS, which indicates that the disturbance condition of small f or large s has little effect on the strength weakening of the specimen. However, with the increase

Sandstone UCT results under different loading conditions

Specimen code	σ_1/MPa	f/Hz	s	σ_p/MPa	(UCS − σ_p)/MPa	SWR/%
16R0-0		0	0	42.98	2.02	4.48
16R3-7		3	0.07s	34.87	10.13	22.51
16R5-7	16	5	0.07s	33.02	11.98	26.62
16R7-7	(36% UCS)	7	0.07s	31.92	13.08	29.06
16R5-12		5	0.12s	36.48	8.52	18.93
16R5-3		5	0.03s	30.23	14.77	32.82
16G0-0		0	0	97.20	2.8	2.80
16G3-7		3	0.07s	85.76	14.24	14.24
16G5-7	16	5	0.07s	82.36	17.64	17.64
16G7-7	(16% UCS)	7	0.07s	79.77	20.23	20.23
16G5-12		5	0.12s	88.24	11.76	11.76
16G5-3		5	0.03s	77.02	22.98	22.98
16P0-0		0	0	146.18	3.82	2.45
16P3-7		3	0.07s	135.24	14.76	9.84
16P5-7	16	5	0.07s	132.63	17.37	11.58
16P7-7	(10%UCS)	7	0.07s	130.96	19.04	12.69
16P5-12		5	0.12s	137.22	12.78	8.52
16P5-3		5	0.03s	129.07	20.93	13.95

of f or the decrease of s, the degree of strength weakening of sandstone increases significantly. For example, when f increases to 5 Hz or s decreases to 0.03 s, the SWR = 32.82% of the red sandstone (16R5-3) specimen is significantly higher than that under the disturbance condition of small f or large s (SWR = 18.93~22.51%).

It is noteworthy that the increase of σ_1 promotes the strength weakening effect of sandstone specimens, and the decrease of σ_p is 18.93%~32.82% UCS when the level of σ_1 is around 30%~40% UCS. However, when the σ_1 level is about 10%~20% UCS, the decrease of σ_p is 8.52%~22.98% UCS, and the decrease of strength is much smaller than that of 30%~40% UCS. It can be seen that SWR is different at different A stress levels, and σ_1 is an intrinsic factor (i.e., it exists on its own and is not an external force). Under the condition of local impact disturbance in deep, highly prestressed rocks, σ_1 is the dominant factor in determining the SWR, and the SWR of the higher (σ_1 = 36% UCS) is significantly higher than that of the lower (σ_1 = 16% or 10% UCS). However, the strength of the specimens decreases more significantly as f increases or s decreases, suggesting that C_c, on the other hand, accelerates the induced rock failure.

4.   Mode of failure

The comparison of UCT failure modes of sandstone with and without local impact disturbance is shown in Fig. 9. The undisturbed specimens are mainly subjected to general shear failure (Fig. 9 (column 1)). However, the sandstone specimen after local impact disturbance produces more fracture surfaces, and conjugate shear failure mainly occurs (Fig. 9 (columns 2-6)), accompanied by tension fracture failure [39]. During the failure process, flaky fragments and debris
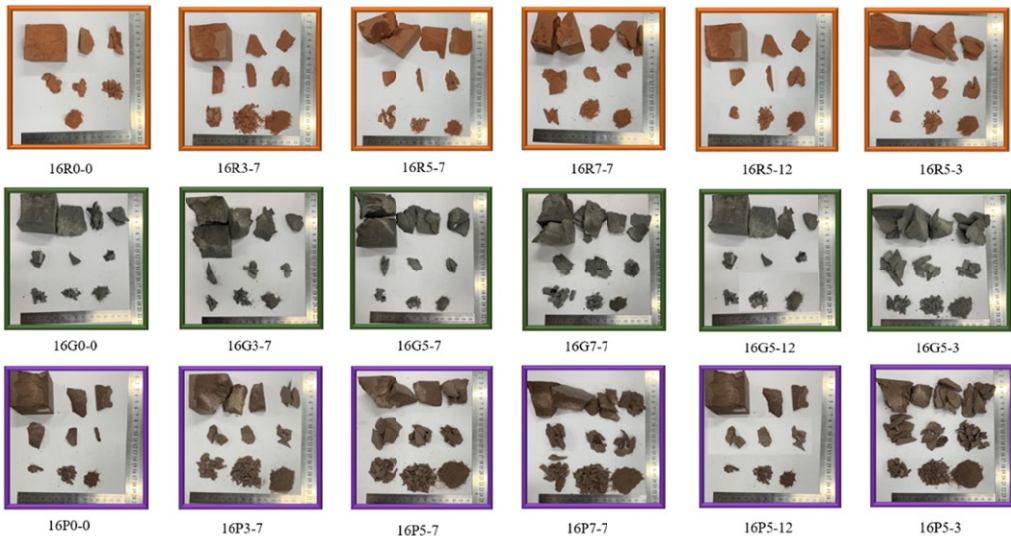
Fig. 9. Macroscopic failure mode of sandstone

are formed, while tension failure produces several strip-shaped fragments, resulting in a higher degree of sandstone fragmentation. In the test, it was also found that the sandstone specimen with higher strength produced a loud sound during the failure process, which is characteristic of typical rock burst failure.

4.1. Crushed rock screening

Rock fragmentation is the result of the continuous generation, propagation and transfixion of internal fractures, and the particle size distribution of rock can effectively evaluate its fragmentation efficiency. However, there are many methods for quantitatively evaluating the degree of rock fragmentation, such as characteristic lumpiness, average lumpiness, fractal dimension, and so on. Among them, fractal dimension has been widely used in the study of rock fragmentation because of its intuitive results and quantitative accuracy. A 0.05~45 mm GZS-300 standard vibrating screen is used for the screening test of the crushed rock. Divide the particle size of the debris into ten grades of 0.05~1 mm, 1~5 mm, 5~10 mm, 10~15 mm, 15~20 mm, 20~25 mm, 25~30 mm, 30~35 mm, 35~40 mm and 40~45 mm, and weigh the mass of the remaining debris on each sieve. It is converted into the cumulative percentage content of rock debris under each sieve aperture, and the curve of debris particle gradation of sandstone after experiencing different disturbance $f - s$ conditions are obtained, as shown in Fig. 10.

The nonuniformity coefficient C_u and curvature coefficient C_c Grading curves are commonly used in engineering to quantify the uniformity and continuity of the particle size distribution, so as to judge the grading quality [41].

$$C_u = \frac{d_{60}}{d_{10}} \tag{2}$$

(a) Red sandstone debris grain gradation

(b) Green sandstone debris grain gradation

(c) Purple sandstone debris grain gradation

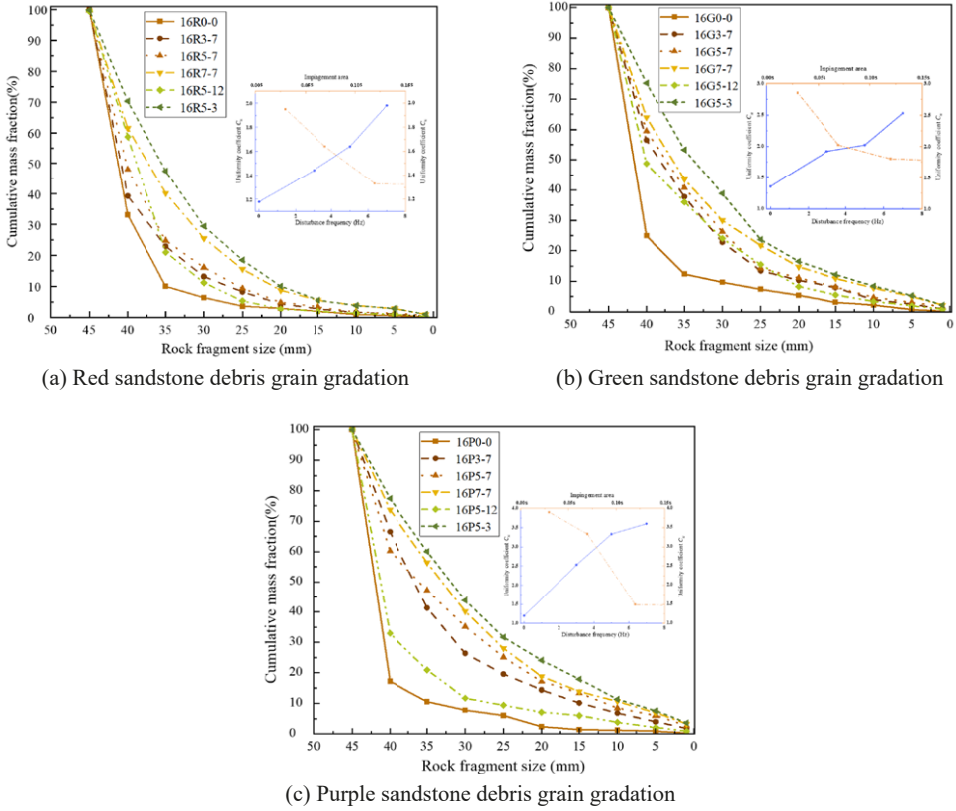Fig. 10. Gradation curves of clastic grains for different $f-s$

$$C_c = \frac{d_{30}^2}{d_{10} \cdot d_{60}} \tag{3}$$

Where: d_{10}, d_{30} and d_{60} denote the particle size corresponding to the mass less than a certain particle size accounting for 10%, 30% and 60% of the total mass, respectively. The grading curve in Fig. 10 can be obtained by the corresponding characteristic particle size, to calculate the nonuniformity coefficient and curvature coefficient of the debris under different working conditions, as shown in TABLE 4.

The results of debris particle gradation show that the cumulative mass fraction curves of sandstone debris disturbed by localized impact show a gradual increase with increasing f or decreasing s, which indicates that the disturbance will lead to the increase of the content of fine particles and the corresponding mass of debris particles. In addition, sieving analysis shows that C_u increases with the increase of f or the decrease of s. The larger the C_u is, the worse the uniformity of the debris is [42], but the C_u of the sandstone under different disturbances is less than 5, indicating that the debris particle size of sandstone is evenly distributed under the action of disturbance load. For example, when f of purple sandstone increases from 3 Hz to 7 Hz, C_u increases from 1.2 to 3.3 (2.75 times that at 3 Hz). When s decreases from 0.12 s to 0.03 s,

Sandstone particle gradation nonuniformity coefficient and curvature coefficient

Rock sample	16R0-0	16R3-7	16R5-7	16R7-7	16R5-12	16R5-3
C_u	1.18	1.44	1.64	1.98	1.33	1.95
C_c	1.04	1.12	1.34	1.78	1.14	1.22
Rock sample	16G0-0	16G3-7	16G5-7	16G7-7	16G5-12	16G5-3
C_u	1.36	1.92	2.02	2.53	1.80	2.85
C_c	1.33	1.24	1.20	1.58	1.16	1.57
Rock sample	16P0-0	16P3-7	16P5-7	16P7-7	16P5-12	16P5-3
C_u	1.20	2.53	3.33	3.6	1.49	3.9
C_c	1.11	1.79	1.57	1.87	1.31	1.98

C_u increases from 1.49 to 3.9 (2.62 times that at 0.12 s), indicating that more fine debris are produced at higher f or smaller s. According to the evaluation standard of particle size distribution, C_c of sandstone samples is between 1 and 3, which indicates that sandstone shows good grain size distribution after crushing, and the trend change of C_c value is the same as that of C_u value.

Based on the particle size analysis of rock samples and the observation of macroscopic failure phenomena, it is shown that the distribution of UCT rock samples is different after the sandstone is subjected to different C_c loading conditions. When small f or large s, the degree of fragmentation of rock samples is low, the continuity is poor, and the main distribution is large debris; while when large f or small s, the degree of fragmentation of rock samples is high, the particle size distribution of debris is uniform, and the continuity is relatively good. To sum up, it shows that the local impact disturbance will promote the damage of rock and further promote the development and penetration of cracks.

4.2. Fractal Dimension Calculation

The block distribution and grain size of crushed rock show good fractal characteristics. The widely used and representative one is the G-G-S (Gate-Gandin-Schuhmann) distribution model [43], and it is generally believed that the G-G-S distribution favors the fine-grained end. The model expression is:

$$Y = (x/x_{max})^a \tag{4}$$

Where: Y represents the cumulative percentage of the mass of the sieved material with a sieve diameter of x, x_{max} is the maximum size of the rock debris, a is the rock debris distribution parameter. Rock fragmentation caused by blasting, impact, vibration or other actions in a wide range of sizes to meet the fractal conditions, block size distribution has fractal characteristics, but to accurately estimate its number is quite difficult if the corresponding mass relationship is more convenient. The fractal dimension D is calculated according to the mass-frequency relationship revealed by the screening test, and the debris distribution equation of sandstone under the action of disturbance load is expressed as [44]:

$$\frac{M(x)}{M_T} = \left(\frac{x}{x_{max}}\right)^{3-D} \tag{5}$$

Where: M_T, $M(x)$ is the total mass of the debris and the cumulative mass under the sieve; x_{max}, x is the maximum debris particle size and particle size; D is the fractal dimension. The natural logarithm is taken on both sides:

$$\ln\left(\frac{M(x)}{M_T}\right) = (3-D)\ln\left(\frac{x}{x_{max}}\right) \tag{6}$$

The slope of the fitted straight line in the $\ln(M(x)/M_T) \sim \ln x$ coordinate of formula (6) is $(3 - D)$, therefore, D can be obtained directly by plotting the slope of the line in double logarithmic coordinates from the statistical analysis of block size.
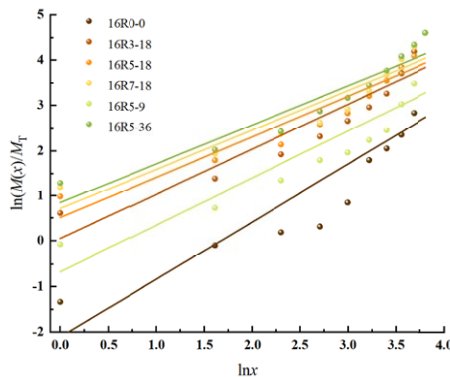
As can be seen from Fig. 11, the percentage of cumulative mass under the sieve of sandstone crushed fragments shows a good linear correlation with the size of the sieve holes in the double
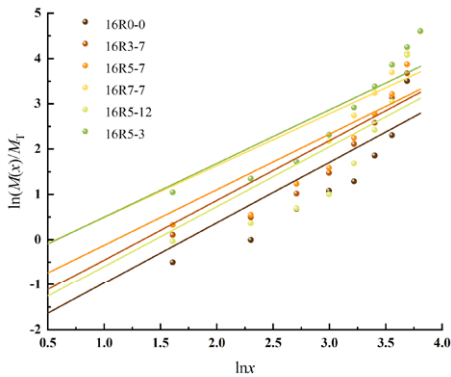
(a) Red sandstone
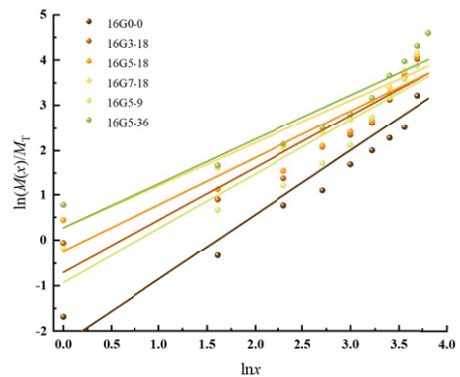
(b) Green sandstone

(c) Purple sandstone

Fig. 11. Fitting curve of sandstone $\ln(M(x)/M_T) \sim \ln x$

logarithmic coordinate system, which indicates that the self-similarity of the block size distribution of the rock samples after crushing is better, i.e., it is a fractal distribution. The macroscopic crushing of rock is formed by the concentration of small fracture groups, which in turn evolve and cluster from even smaller fractures, and since the self-similarity behaviour will make the block size of the crushed fragments also have self-similar characteristics, the degree of crushing of rock specimens can be quantitatively characterised by D [45].

According to the slope of the fitted straight line in the above curves, D of each rock sample under different perturbation conditions is obtained as shown in TABLE 5, and the change of D represents to some extent the change of the internal properties of sandstone UCT crushing with the change of local impact perturbation. The fractal dimension of the crushed rock mass by local impact disturbance fluctuates up and down in a certain range, and the fractal dimension of the red sandstone mass is concentrated in the range of 1.68~1.86, the green sandstone is mainly concentrated in the range of 1.8~2.02, and the purple sandstone is mainly concentrated in the range of 1.97~2.14. It can be seen that the D of different kinds of sandstone is not only related to the degree of disturbance but also closely related to the nature of the rock itself [46].

TABLE 5

Statistical results of D

Rock samples	16R0-0	16R3-18	16R5-18	16R7-18	16R5-9	16R5-36
Slope	1.33	1.32	1.22	1.14	1.32	1.18
D	1.67	1.68	1.78	1.86	1.68	1.82
R^2	0.76	0.82	0.78	0.84	0.74	0.85
Rock samples	16G0-0	16G3-18	16G5-18	16G7-18	16G5-9	16G5-36
Slope	1.42	1.15	1.04	0.95	1.2	0.98
D	1.58	1.85	1.96	2.05	1.8	2.02
R^2	0.88	0.87	0.83	0.87	0.86	0.89
Rock samples	16P0-0	16P3-18	16P5-18	16P7-18	16P5-9	16P5-36
Slope	1.27	0.99	0.89	0.87	1.03	0.86
D	1.73	2.01	2.11	2.13	1.97	2.14
R^2	0.76	0.87	0.88	0.88	0.81	0.91

Fig. 12 shows the relationship between the fractal dimension of UCT sandstone and the change in local impact disturbance. The three kinds of sandstone D show a slow upward trend with the increase of f or the decrease of s. Under the same $f - s$ condition, purple sandstone $D >$ green sandstone $D >$ red sandstone D, but the fractal dimension-disturbance relationship curve of red sandstone is more discreet than that of purple sandstone and green sandstone. Through the combination of fractal dimension and macroscopic failure of sandstone specimens, it is found that the red sandstone specimens with small fractal dimension have a small number of fragments, a large size, a relatively low degree of fragmentation, and a poor uniformity of fragmentation. On the contrary, the purple sandstone specimens with large fractal dimensions have a large number of fragments, a small size, a high degree of fragmentation, and a good uniformity of fragmentation. The reason is that due to the high strength of purple sandstone, rockburst occurs during the failure process and more debris is produced [47].
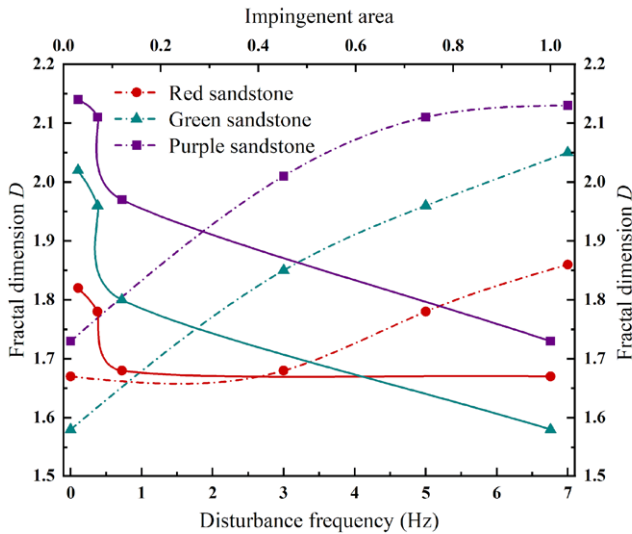
Fig. 12. Sandstone $D - f - s$ variation relationship

5. Conclusions

In this study, uniaxial compression and acoustic emission tests were conducted on deep sandstone specimens after experiencing different localized impact disturbances to investigate the effects of dynamic impact disturbances on the uniaxial mechanical properties and failure modes of sandstones. The study draws the following conclusions:

(1) The stress curve during UCT loading can be divided into four stages: initial crack compaction, elastic deformation, unstable crack extension and damage, and each stage roughly corresponds to the initial silence period, random distribution period, aggregated burst period and failure reduction period of the acoustic emission event. Sandstone through many local impact disturbances will make its peak stress decrease, the generation of acoustic emission signals in the early stage plays a certain role in promoting, and with the increase in the frequency of disturbance or impact area reduction, the more significant this promotion effect.

(2) High prestress local impact disturbance has an obvious strength-weakening effect on sandstone. High prestress is the premise and dominant factor of sandstone strength weakening. The higher the prestress level, the more obvious the strength-weakening effect. The power impact disturbance will accelerate the sandstone failure, the macroscopic failure mode is conjugate shear failure with tensile cracking, and the more intense the disturbance degree, the more obvious the strength weakening effect.3-7 Hz disturbance frequency or 0.03 s-0.12 s impact area will make the strength of sandstone reduced by 8.52% to 32.82%.

(3) The fractal dimension can be used to quantitatively evaluate the crushing characteristics of rocks, and the particle size distribution of sandstone fragments crushed by local impact perturbation follows a fractal relationship. With the increase of perturbation frequency

or the decrease of impact area, the fractal dimension of UCT sandstone damage shows a good linear increasing trend between 1.68 and 2.14, with a high degree of fragmentation and good block size uniformity. Therefore, the study of the failure mode can provide a new research way to explore the intrinsic law between the fractal characteristics and mechanical properties of rock dynamically disturbed crushing.

Highlights

[1] High prestress local impact disturbance has an obvious strength-weakening effect on sandstone

[2] High prestress is the premise and dominant factor of sandstone strength weakening, and the disturbance will accelerate the sandstone failure

[3] Each stage of the uniaxial compression test stress curve corresponds to each stage of the acoustic emission event

[4] The particle size distribution of sandstone fragments crushed by local impact perturbation follows a fractal relationship

Acknowledgments

Author contributions

All authors contributed to the study conception and design. Material preparation, data collection and analysis were performed by [Yanfeng Li], [Pengfei Wu], [Haibo Wang] and [Yingshuang Shi]. The first draft of the manuscript was written by [Jihe Zhao], [Jiaxu Jin] and all authors commented on previous versions of the manuscript. All authors read and approved the final manuscript.

Data Availability Statement (DAS)

The data that support the findings of this study are available from the corresponding author, [Jiaxu Jin], upon reasonable request.

References

[1] R.P. Young, D.S. Collins, Seismic studies of rock fracture at the Underground Research Laboratory, Canada. Int. J. Rock. Mech. Min. **38** (6), 787-799 (2001). DOI: https://doi.org/10.1016/S1365-1609(01)00043-0

[2] L.M. Dou, Z. Mu, Z. Li, Research progress of monitoring, forecasting, and prevention of rockburst in underground coal mining in China. Int. J. Coal. Sci. Tech. **1** (003), 278-288 (2014).
DOI: https://doi.org/10.1007/s40789-014-0044-z

[3]   C.H. Dowding, C.A. Andersson, Potential for rock bursting and slabbing in deep caverns. Eng. Geol. **22** (3), 265-79 (1986). DOI: https://doi.org/10.1016/0013-7952(86)90028-1

[4]   C. Li, Y.Q. Hu, T. Meng, P.H. Jin, Z.R. Zhao, C.W. Zhang, Experimental study of the influence of temperature and cooling method on mechanical properties of granite: implication for geothermal mining. Energy. Sci. Eng. **8** (5), 1716-1728 (2020). DOI: https://doi.org/10.1002/ese3.627

[5]   H. Xu, G. Wang, Y.Y. Guo, B. Chang, Y.W. Hu, J.Y. Fan, Theoretical, numerical, and experimental analysis of effective extraction radius of coalbed methane boreholes by a gas seepage model based on defined criteria. Energy Sci. Eng. **8** (3), 880-97 (2020). DOI: https://doi.org/10.1002/ese3.557

[6]   Z. Zhao, X. Gao, S. Chen, M.Z. Zhang, W. Sun, Coupling model of disk splitting for expansive rock mass in deep storage considering water infiltration. Energy Sci. Eng. **8** (9), 3200-16 (2020).
DOI: https://doi.org/10.1002/ese3.729

[7]   M. Zheng, S. Li, H. Xu, Z. Liang, X. Lu, Investigation of the rock failure effect on overcoring stress relief test in deep hard rock. B. En. Geol. Environ. **82** (9), 353 (2023).
DOI: https://doi.org/10.1007/s10064-023-03377-z

[8]   C. Zang, M. Chen, G. Zhang, K. Wang, D. Gu, Research on the failure process and stability control technology in a deep roadway: Numerical simulation and field test. Energy Sci. Eng. **8** (7), 2297-2310 (2020).
DOI: https://doi.org/10.1002/ese3.664

[9]   S. Gómez, J.A. Sanchidrián, P. Segarra, Near-field vibration from blasting and rock damage prediction with a full-field solution. Int. J. Rock. Mechanic. Min. **134**, 104357 (2020).
DOI: https://doi.org/10.1016/j.ijrmms.2020.104357

[10] C.S. Ma, W.Z. Chen, X.J.Tan, H.M. Tian, J.P. Yang, J.X. Yu, Novel rockburst criterion based on the TBM tunnel construction of the Neelum–Jhelum (NJ) hydroelectric project in Pakistan. Tunn. Undergr. Sp. Tech. **81**, 391-402 (2018). DOI: https://doi.org/10.1016/j.tust.2018.06.032

[11] X. Li, Z. Zhou, T.S. Lok, L. Hong, T. Yin, Innovative testing technique of rock subjected to coupled static and dynamic loads. Int. J. Rock. Mechanic. Min. **45** (5), 739-748 (2008). DOI: https://doi.org/10.1016/j.ijrmms.2007.08.013

[12] F. Gong, X. Li, X. Liu, J. Zhao, Experimental study of dynamic characteristics of sandstone under one-dimensional coupled static and dynamic loads. Chi. J. Rock. Mech. Eng. **29** (10), 2076-2085 (2010).
DOI: https://doi.org/10.15407/fm25.01.122

[13] D. Luo, G. Su, G. Zhang, True-triaxial experimental study on mechanical behaviours and acoustic emission characteristics of dynamically induced rock failure. Rock. Mech. Rock. Eng. **53** (3), 1205-1223 (2020).
DOI: https://doi.org/10.1007/s00603-019-01970-x

[14] Z. Zhou, X. Cai, X. Li, W. Cao, X. Du, Dynamic response and energy evolution of sandstone under coupled static–dynamic compression: insights from experimental study into deep rock engineering applications. Rock. Mech. Rock. Eng. **53**, 1305-1331 (2020). DOI: https://doi.org/10.1007/s00603-019-01980-9

[15] S.H. Li, W.C. Zhu, L.L. Niu, M. Yu, C.F. Chen, Dynamic characteristics of green sandstone subjected to repetitive impact loading: phenomena and mechanisms. Rock. Mech. Rock. Eng. **51**, 1921-1936 (2018).
DOI: https://doi.org/10.1007/s00603-018-1449-6

[16] Y. Xia, H. Zhou, C. Zhang, S. He, Y. Gao, P. Wang, The evaluation of rock brittleness and its application: a review study. Eur. J. Environ. Ci. Eng. **26** (1), 239-279 (2022).
DOI: https://doi.org/10.1080/19648189.2019.1655485

[17] Z. Wang, L. Dou, G. Wang, J. He, J. Hu, Failure Mechanism of Anchored Roadway Surrounding Rocks under Near-Field Dynamic Disturbance. KSCE. J. Civ. Eng. **2024**, 1-15 (2024).
DOI: https://doi.org/10.1007/s12205-024-1813-x

[18] Y. Xi, H. Wang, J. Li, W. Dong, H. Li, B. Guo, Experimental comparison of mechanical properties and fractal characteristics of geothermal reservoir rocks after different cooling treatments. Energy Rep. **8**, 5158-5176 (2022).
DOI: https://doi.org/10.1016/j.egyr.2022.03.207

[19] H. Li, X. Li, J. Fu, N. Zhu, D. Chen, Y. Wang, Experimental study on compressive behavior and failure characteristics of imitation steel fiber concrete under uniaxial load. Constr. Build. Mater. **399**, 132599 (2023).
DOI: https://doi.org/10.1016/j.conbuildmat.2023.132599

[20] J. Hao, L. Qiao, Q. Li, Study on cross-scale pores fractal characteristics of granite after high temperature and rock failure precursor under uniaxial compression. Powder Technol. **401**, 117330 (2022).
DOI: https://doi.org/10.1016/j.powtec.2022.117330

[21] Y. Wang, C.H. Li, H. Liu, Fracture failure analysis of freeze–thawed granite containing natural fracture under uniaxial multi-level cyclic loads. Theor. Appl. Fract. Mec. **110**, 102782 (2020).
DOI: https://doi.org/10.1016/j.tafmec.2020.102782

[22] Y. Lai, K. Zhao, Z. He, X. Yu, Y. Yan, Q. Li, Y. Zhou, Fractal characteristics of rocks and mesoscopic fractures at different loading rates. Geo. Energy Environ. **33**, 100431 (2023).
DOI: https://doi.org/10.1016/j.gete.2022.100431

[23] Y. Wang, R. Liu, H. Ji, S. Li, L. Yu, X. Feng, Correlating mechanical properties to fractal dimensions of shales under uniaxial compression tests. Environ. Earth Sci. **82** (1), 2 (2023).
DOI: https://doi.org/10.1007/s12665-022-10642-z

[24] X.T. Feng, B. Haimson, X. Li, C. Chang, X. Ma, X. Zhang, K. Suzuki, ISRM suggested method: determining deformation and failure characteristics of rocks subjected to true triaxial compression. Rock Mech. Rock Eng. **52**, 2011-2020 (2019). DOI: https://doi.org/10.1007/s00603-019-01782-z

[25] C.E. Fairhurst, J.A. Hudson, Draft ISRM suggested method for the complete stress-strain curve for intact rock in uniaxial compression. Int. J. Rock Mechanic. Min. **36** (3), 279-289 (1999).
DOI: https://doi.org/10.1007/978-3-319-07713-0_15

[26] E. ISRM, Rock characterization, testing and monitoring – ISRM suggested methods. Suggest. methods Quant. Descr. discontinuities rock masses, **1891**, 3-52 (1981).

[27] T. Zhao, P. Zhang, Y. Xiao, W. Guo, Y. Zhang, X. Zhang, Master crack types and typical acoustic emission characteristics during rock failure. Int. J. Coal Sci. Tech. **10** (1), 2 (2023).
DOI: https://doi.org/10.1007/s40789-022-00562-5

[28] M. Jia, K. Qian, K. Yu, Acoustic Emission Characteristics and Failure Patterns of Basalt Fiber and Basalt Textile Reinforced Concrete under Flexural Load. J. Nat. Fibers **19** (16), 14725-14743 (2022).
DOI: https://doi.org/10.1080/15440478.2022.2068728

[29] C.H. Ren, J. Yu, X.Y. Liu, Z.Q. Zhang, Y.Y. Cai, Cyclic constitutive equations of rock with coupled damage induced by compaction and cracking. Int. J. Min. Sci. Tech. **32** (5), 1153-1165 (2022).
DOI: https://doi.org/10.1016/j.ijmst.2022.06.010

[30] L. Gori, S.S. Penna, R.L. da Silva Pitangueira, Discontinuous failure in micropolar elastic-degrading models. Int. J. Damage Mech. **27** (10), 1482-1515 (2018). DOI: https://doi.org/10.1177/1056789517731137

[31] D. Krajcinovic, M.A.G Silva, Statistical aspects of the continuous damage theory. Int. J. Solids Struct. **18** (7), 551-562 (1982). DOI: https://doi.org/10.1016/0020-7683(82)90039-7

[32] X. Wang, J. Lai, S. He, R.S. Garnes, Y. Zhang, Karst geology and mitigation measures for hazards during metro system construction in Wuhan, China. Nat. Hazards **103**, 2905-2927 (2020).
DOI: https://doi.org/10.1007/s11069-020-04108-3

[33] Y. Gao, D. Lan, S. Yang, P. Hou, Y. Wang, F. Ding, The acoustic emission behavior and its fractal characteristics of the sandstone under the disturbance stress paths. Rock Mech. Rock Eng. **56** (8), 5487-5511 (2023).
DOI: https://doi.org/10.1007/s00603-023-03342-y

[34] Z. Zhao, H. Liu, Q. Ma, J. Shang, Micro-macro damage, deterioration and cracking of heterogeneous composite rock masses with non-penetrating cracks under uniaxial compression. Theor. Appl. Fract. Mec. **125**, 103919 (2023).
DOI: https://doi.org/10.1016/j.tafmec.2023.103919

[35] F. Zhao, Y. Li, Z. Ye, Y. Fan, S. Zhang, H. Wang, Y. Liu, Research on acoustic emission and electromagnetic emission characteristics of rock fragmentation at different loading rates. Shock. Vib. **2018**, 4680879 (2018).
DOI: https://doi.org/10.1155/2018/4680879

[36] Y. Lai, K. Zhao, Z. He, X. Yu, Y. Yan, Q. Li, Y. Zhou, Fractal characteristics of rocks and mesoscopic fractures at different loading rates. Geomech. Energy Environ. **33**, 100431 (2023).
DOI: https://doi.org/10.1016/j.gete.2022.100431

[37] S. Li, D. Yang, Z. Huang, Q. Gu, K. Zhao, Acoustic emission characteristics and failure mode analysis of rock failure under complex stress state. Theor. Appl. Fract. Mec. **122**, 103666 (2022).
DOI: https://doi.org/10.1016/j.tafmec.2022.103666

[38] M. Hu, Z. Zhang, Y. Yin, B. Huang, S. Yu, Y. Liao, Study on strength weakening of carbonate rocks with water level fluctuating in Wuxia of Three Gorges Reservoir area. J. Eng. Geo. **31** (5), 1615-1627 (2023).
DOI: https://doi.org/10.1109/mace.2011.5987758

[39] P. Deng, Q. Liu, H. Lu, FDEM numerical study on the mechanical characteristics and failure behavior of hetero-geneous rock based on the Weibull distribution of mechanical parameters. Comput. Geotech. **154**, 105138 (2023). DOI: https://doi.org/10.1016/j.compgeo.2022.105138

[40] Z. Liu, J. Shao, W. Xu, Y. Meng, Prediction of rock burst classification using the technique of cloud models with attribution weight. Nat. Hazards **68**, 549-568 (2013). DOI: https://doi.org/10.1007/s11069-013-0635-9

[41] ASTM D6913/D6913M-17, Standard test methods for particle-size distribution (gradation) of soils using sieve analysis. ASTM Int. (2017)

[42] K. Zeng, H. Liu, Effect of particle size distributions on the mechanical behavior and particle breakage of coral sands. Granul. Matter. **25** (3), 44 (2023). DOI: https://doi.org/10.1007/s10035-023-01334-x

[43] X.Y. Tian, F.J. Zhao, W.J. Wang, B. Chen, Y.J. Ma, B.J. Fan, Study on energy evolution and fractal characteristics of sandstone with different fracture dip angles under uniaxial compression. Sci. Rep.-UK. **14** (1), 10464 (2024). DOI: https://doi.org/10.1038/s41598-024-60902-0

[44] L. Li, W. Wu, M.H. El Naggar, G. Mei, R. Liang, Characterization of a jointed rock mass based on fractal geometry theory. B. Eng. Geol. Environ. **78**, 6101-6110 (2019). DOI: https://doi.org/10.1007/s10064-019-01526-x

[45] X.F. Li, H.B. Li, Q.B. Zhang, J.L. Jiang, J. Zhao, Dynamic fragmentation of rock material: characteristic size, fragment distribution and pulverization law. Eng. Fract. Mech. **199**, 739-759 (2018). DOI: https://doi.org/10.1016/j.engfracmech.2018.06.024

[46] L. Hu, Z. Zhang, X. Liang, C. Tang, Fractal Analysis of Fragmentation Distribution of Rockbursts Induced by Low-Frequency Seismic Disturbances. Adv. Civ. Eng. **2021**, 1-14 (2021). DOI: https://doi.org/10.1155/2021/6679891

[47] T. Cheng, M. He, H. Li, D. Liu, Y. Qiao, J. Hu, Experimental investigation on the influence of a single structural plane on rockburst. Tunn. Undergr. Sp. Tech. **132**, 104914 (2023). DOI: https://doi.org/10.1016/j.tust.2022.104914